Advances in Science and Technology
Research Journal

Advances in Science and Technology Research Journal, 2026, 20(8), 387–396
https://doi.org/10.12913/22998624/221558
ISSN 2299-8624, License CC-BY 4.0

Received: 2026.04.23
Accepted: 2026.06.01
Published: 2026.07.01

Design of the microcontroller system based solar station with folding photovoltaic modules

Gagik Tigran Kirakossian[1], Gagik Hrachik Kirakosyan[1], Ovsanna Ashot Zadoyan[1*]

[1] National Polytechnic University of Armenia, 105 Teryan Str., Yerevan, Armenia
* Corresponding author's e-mail: ovsanna.zadoyan@polytechnic.am

ABSTRACT

This paper presents the design, modeling, and control optimization of a solar station equipped with automatically folding photovoltaic (PV) modules operated by a microcontroller-based feedback system. The system performs in two modes: an opening mode that deploys the PV modules to maximize solar exposure for efficient energy harvesting, and a closing mode that retracts the modules to reduce aerodynamic drag and improve mobility. Such a dual-mode architecture makes the proposed solution suitable for compact robotic platforms and electric vehicles that require adaptive PV configurations. A complete kinematic and dynamic model of the folding mechanism is developed. A proportional–integral–derivative controller is designed and optimized to enhance response characteristics. Bode and step-response analyses confirm that the controller increases system robustness by ensuring high stability margins while maintaining rapid dynamic performance.

Keywords: damping coefficient, folding photovoltaic modules, proportional–integral–derivative controller, solar station, transfer function.

INTRODUCTION

Robots and electric vehicles (EVs) are becoming increasingly widespread in modern industries, logistics, agriculture, medicine, and emergency-response operations due to their environmental compatibility, high mobility, and operational efficiency [1–9]. Despite these advantages, the autonomy of such platforms is limited by the restricted capacity of onboard batteries, which require periodic returns to stationary charging units and interrupt long-duration missions. This challenge becomes especially critical in mobile robotic systems operating in remote environments, where access to conventional charging infrastructure is limited.

To address these limitations, a growing research direction focuses on integrating photovoltaic (PV) energy-harvesting systems into mobile platforms. Recent studies have demonstrated that PV-assisted charging can significantly extend mission duration, reduce dependency on grid-based charging, and increase operational flexibility [10]. Movable, deployable or folding PV structures have attracted substantial attention in this context due to their ability to dynamically change geometry, reduce aerodynamic drag during motion, and maximize solar exposure during charging [11]. Such folding mechanisms are particularly suited for portable, autonomous, or compact mechatronic systems, where available surface area is limited and structural adaptability is essential [1].

Parallel to these developments, advances in battery technologies have further strengthened the feasibility of mobile solar stations. Solid-state batteries featuring high energy density, improved safety, and ultra-fast charging characteristics have become promising candidates for integration with PV-powered robotic and EV platforms [12–17]. When combined with intelligent solar energy harvesting, such batteries enable rapid recharge cycles, making folding PV systems a practical solution for autonomous applications requiring frequent energy replenishment.

In addition to structural innovations, numerous research efforts emphasize the importance of intelligent control in increasing the power efficiency of PV systems. Studies on solar tracking systems, dynamic adjustment of PV angles, and mechatronic actuation strategies confirm that advanced control algorithms can significantly enhance power output and system performance [18–24]. However, implementing folding or reconfigurable PV systems introduces additional challenges, including nonlinear joint dynamics, oscillatory responses, and sensitivity to disturbances. Classical PI controllers often fail to adequately suppress oscillations or achieve zero steady-state error in such electromechanical systems.

Recent works indicate that optimized PID controllers provide superior results in similar mechatronic applications, offering reduced oscillations, improved damping, faster settling time, and better robustness under variable mechanical loading [25–26]. Nevertheless, despite significant progress in control strategies for solar tracking and actuator systems, a comprehensive dynamic analysis dedicated specifically to folding PV modules and their microcontroller-based actuation remains limited in the literature. Existing studies typically focus either on static PV orientation mechanisms or on battery-charging optimization without considering the combined kinematic and dynamic characteristics of deployable PV structures.

Motivated by these gaps, the present work aims to develop, model, and optimize a complete microcontroller-based actuation system for solar stations equipped with automatically folding PV modules. The study includes a detailed kinematic description of the folding mechanism, a dynamic representation of the DC motor and its load, and the design of an optimized PID controller tailored to the specific electromechanical characteristics of the system. MATLAB-based simulations – including Bode analysis, stability margin evaluation, and transient response characterization – are used to assess the effectiveness of the proposed control approach. Special emphasis is placed on eliminating high-frequency oscillations, improving settling time, and ensuring zero steady-state error, which are essential for reliable operation of mobile folding PV structures.

The novelty of this research lies in the development of a unified and optimized control architecture dedicated to automatically folding PV systems for mobile robotic platforms and electric vehicles. Unlike previous works that primarily address solar tracking or fixed-panel control, this study provides a complete dynamic and control-theoretic analysis of the folding mechanism itself. The results demonstrate substantial improvements in system stability, positioning speed, and robustness, contributing to the development of compact, adaptive, and energy-efficient solar stations for next-generation mobile energy platforms.

The goal of this work is to develop a microcontroller system based on a new method to improve the efficiency and stability of solar stations with opening and closing PV modules.

This work provides a complete dynamic model, stability-margin assessment, and a MATLAB-based PID optimization framework for the actuation of folding PV modules. Such a comprehensive control-oriented analysis has not been previously applied to mobile solar stations with automatically opening and closing photovoltaic structures.

METHODS

Kinematic model of the automatically opening and closing equipment

The general structure of the solar station with folding photovoltaic modules is illustrated in Figure 1. A simple application of a DC motor is the PV modules drive mechanism in a opening-closing equipment as shown in Figure 1.

Figure 2 shows the opening-closing equipment, which consists of two links (solar modules) and one joint. The first solar module is stationary, while the second one moves relative to the first through the joint, where a constant current motor is located. The angle formed between the first and second modules, or the joint angle, is denoted by θ.

The coordinates of the endpoint of the second module (x_1, x_2) are given by the following formulas: $x_1 = L \cos \theta$, $x_2 = L \sin \theta$ where L is the length of the PV module.

The angular displacement of the second solar module is described by the polynomial function given in Equation 1.

$$\theta(t) = a_0 + a_1 t^5 + a_2 t^4 + \\ + a_3 t^3 + a_4 t^2 + a_5 t \tag{1}$$

where: $a_0 = \theta(0)$ is the initial angle at time t = 0, and the vector of coefficients

$\vec{a} = [a_1, a_2, a_3, a_4, a_5]^{\mathrm{T}}$ is determined based on the condition to ensure the desired trajectory of the endpoint of the second module. The angular velocity and angular acceleration at time t =0 are also equal to zero, which implies that $a_4 = a_5 = 0$.

Given the initial coordinates of the endpoint of the second module at t = 0 and the desired final coordinates of the endpoint of the second module at t =t_f, the required value of the angle $\theta(t_f)$ can be found using trigonometric expressions.

Taking into account, that $\theta'(t_f) = \theta''$, the linear system given in Equation 2 is obtained.

$$\begin{bmatrix} t_f^5 & t_f^4 & t_f^3 \\ 5t_f^4 & 4t_f^3 & 3t_f^2 \\ 20t_f^3 & 12t_f^2 & 6t_f \end{bmatrix} \begin{bmatrix} a_1 \\ a_2 \\ a_3 \end{bmatrix} = \begin{bmatrix} \theta(t_f) \\ 0 \\ 0 \end{bmatrix} \tag{2}$$

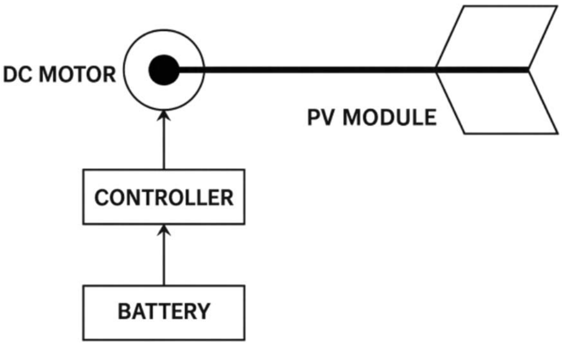

Figure 1. Schematic representation of the solar station with folding photovoltaic modules

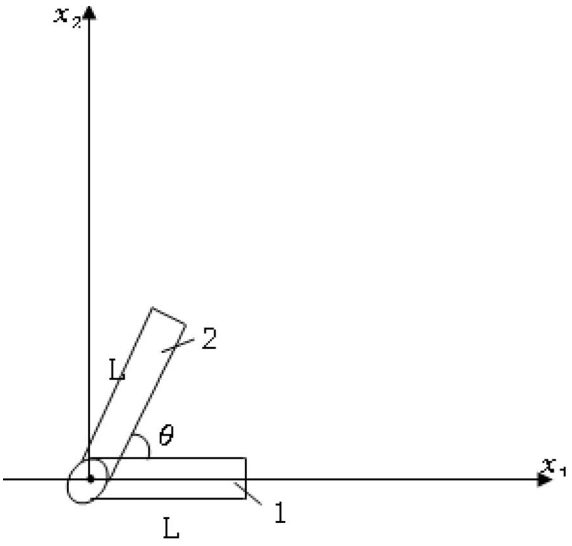

Figure 2. Schematic view of the solar modules opening equipment

Note that we obtained three equations with three unknowns for the angle θ and its two derivatives. This is why we chose a fifth-degree polynomial motion to control the movement. The lower-order terms (t^2, t^1, t^0) have zero coefficients in order to satisfy the constraints a t = 0. After eliminating the lower-order terms, we are left with higher-order terms (t^5, t^4, t^3) with their corresponding unknown coefficients. The addition of higher-order terms would require additional constraint equations to be able to calculate the corresponding coefficients.

Folding PV modules have been demonstrated to significantly improve maneuverability in dynamic robotic applications while preserving surface exposure during stationary charging cycles [11].

MATLAB is used to find the control coefficients for the motion of the opening equipment, as well as to calculate and construct the trajectory of the second module's endpoint [27]. The fragment of the MATLAB program is as follows:

- Endpoint of the second solar module for opening system.
- Initial values, angles in degrees.
- Here, tf defines the total duration of the motion (2 seconds), theta0 is the initial joint angle (0 radians), and thetatf is the final angle (π radians), representing a 180° rotation. tf=2; theta0=0; thetatf=pi.
- Equations for the coefficients.
- These lines compute the coefficients of a 5th-order polynomial that ensures smooth angular motion of the PV module between the initial and final positions.
  - T=[tf^5 tf^4 tf^3
  - 5·tf^4 4·tf^3 3·tf^2
  - 20·tf^3 12·tf^2 6·tf];
  - c=[thetatf;0;0]; disp('Coefficients for theta motion:'); a=T\c.
- Equations of motion.
- The following lines define the module length (L), generate a time vector (t), and compute the angular position (theta) and Cartesian coordinates (x1, x2) of the module endpoint over time.
  L=30; t=linspace(0,2,401); tq=[t.^5;t.^4;t.^3]; theta=a'·tq; x1=L·cos(theta); x2=L·sin(theta).

The trajectory of the second module's endpoint is shown in Figure 3.

In principle, solar stations with closing PV modules are not different from those with opening PV modules.

The dynamic model of the automatically opening-closing equipment

Let's consider the positioning system of the second module of the opening-closing equipment for solar modules, which is described by the transfer function given in Equation 3 [1].

$$\frac{\omega(s)}{V(s)} = G_v(s) = \frac{K}{(R + Ls)(Js + b) + K^2} \tag{3}$$

where: *R* is the active resistance of the armature circuit*, L* is the inductance of the armature circuit, *b* is the damping coefficient of the mechanical system, *K* is the electromagnetic moment coefficient of the motor, and *J* is the total inertia moment of the armature and load.

The output value ω (s) is the angular velocity of the second solar module, while the input value *V*(s) is the voltage supplying the DC motor's armature located at the joint. The following parameters of the DC motor are used:

– $J = 0.04$ kg · m^2*,* $b = 9.7$ Nms,

– $K = 3$ Nm/A, R = 40 Ω.

After executing the command *damp*, the poles, natural frequencies, and damping coefficients for this second-order equipment are obtained. The open-loop system parameters and corresponding dynamic characteristics are summarized in Table 1.

It is clear that the damping coefficient is very small, and therefore, the positioning system of the second solar module will experience quite a few oscillations before reaching the desired value of ω_d(s). Since the object is of type 0, the steady-state error caused by the transitional input signal will not be zero. In the case of a step input, to make the steady-state error zero, we preselect a PID microcontroller with the following coefficients: $K_D = 0$, $K_P = 1$, and $K_I = 1100$, resulting in the transfer function for the microcontroller given in Equation 4.

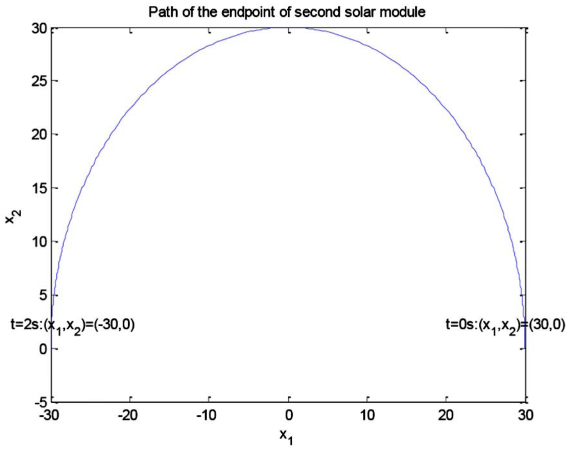

Figure 3. The calculated trajectory of the second module's endpoint

$$C(s) = \frac{s + 1100}{s} \tag{4}$$

Since *C*(s) does not have a derivative term; it is simply a proportional-integral (PI) microcontroller, with the zero at s = -1100 and the pole at s = 0. By connecting *C*(s) and *G*(v) in series and closing the feedback loop as shown in Figure 4, we obtain the following transfer function for the microcontroller system.

$$\frac{\omega(s)}{\omega_d(s)} = \frac{700s + 770000}{s^3 + 15s^2 + \\ + 100700s + 770000} \tag{5}$$

The Bode diagrams for the *G*(v) equipment, *C*(s) microcontroller, and the microcontroller system can be obtained using the following commands [27]:

- `>>G=tf (num, den); w=logspace (-1, 4); [mag1, phase1, w] = bode (G, w);`
- `>>n1= [1 1100]; d1 = [1 0]; C=tf (n1, d1); [mag2, phase2, w] =bode (C, W);`
- `>>nCL=[700 770000]; dCL=[1 15 100700 770000]; GCL=tf(nCL,dCL) ;`
- `>> [mag3, phase3, w] =bode (GCL, w);`

The calculated Bode diagrams are shown in Figure 5. It is evident that the PI microcontroller increases the gain factor while simultaneously reducing the phase at low frequencies, and does not change the gain factor at high frequencies.

The microcontroller system's gain factor for the constant current is reduced to 0 decibels, indicating that the transient response will have zero steady-state error. There is a reduction in the gain factor at low frequencies in the feedback system due to the increased gain, which indicates a loss of stability compared to the observed object. The object's natural frequency is 316.23 rad/s, which is visible as the maximum gain factor on the graph.

Table 1. Open-loop system poles and damping

Eigenvalue	Damping	Freq.(Rad/s)
-7.5000e+000+3.1614e+002i	2.371e-002	3.1623e+002
-7.5000e+000-3.1614e+002i	2.371e-002	3.1623e+002

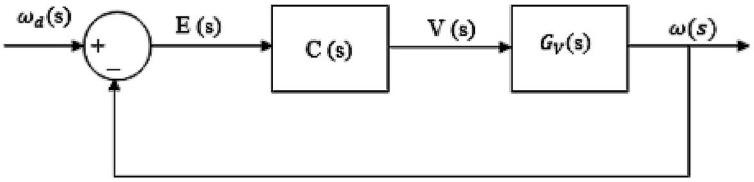

Figure 4. The closed-loop microcontroller system with transfer functions C(s) and *G*(v) (s)

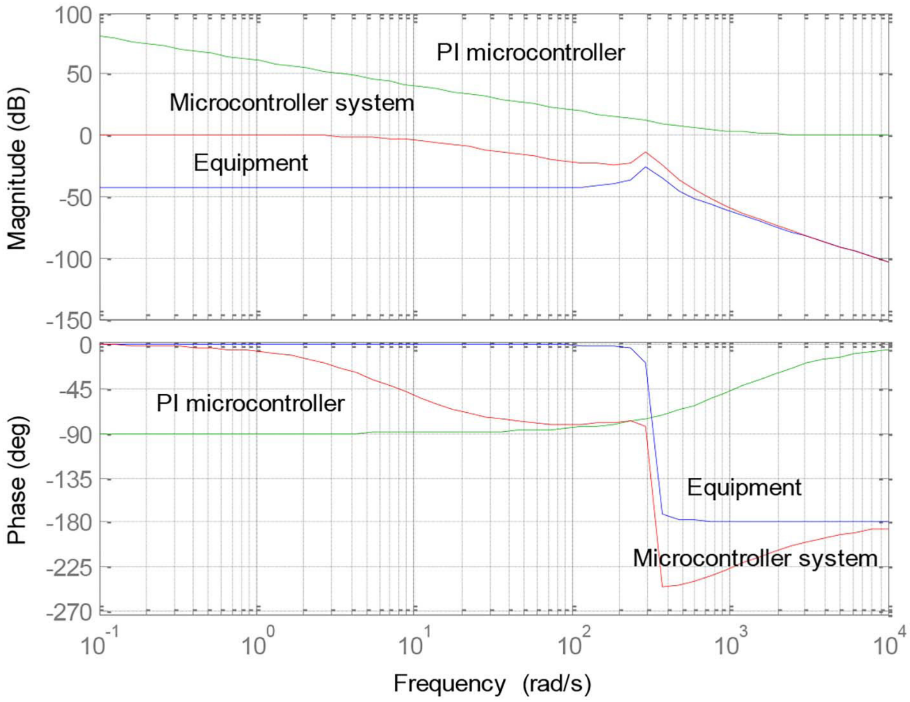

Figure 5. Bode diagrams of the equipment, PI microcontroller, and the microcontroller system for the solar module opening-closing equipment

The poles of the closed-loop microcontroller system are obtained as shown in Table 2.

It should be noted that the damping coefficient of the feedback system slightly decreases near the object's natural frequency, while the other pole is located at s=−7.6507. The step responses are calculated using the stepresp.m M-file and by executing the following commands.

- >> [s1, t] = stepresp (num, den, 0, 0.01, 1);
- >> [s2, t] = stepresp (nCL, dCL, 0, 0.01, 1);

The comparison of these two-step responses is shown in Figure 6. It should be noted that the object's positioning time and the number of oscillations do not change, even when the steady-state error of the microcontroller system is zeroed [28].

In addition, we can compare the gain and phase margins of the microcontroller system and the object to see how stability changes. The gain and phase margins of the object, along with the corresponding crossover frequencies, are calculated using the margin command in the following way.

- >> [gm, pm, wg, wp] =margin (G) gm = Inf, Pm = Inf, wg = NaN, wp = NaN

Thus, the object has infinite reliability margins in terms of gain and phase, and as a result, the corresponding crossover frequencies are undefined. The reliability margins of the microcontroller system can be calculated as follows:

- >> [gmCL, pmCL, wgCL, wpCL] = margin (GCL)
- gmCL = 0.9750, pmCL= -3.8267, wgCL= 318.4062, wpCL = 318.6843

The gain and phase margins of the microcontroller system have significantly decreased to 0.975 (-0.22 dB) and -3.8267°, respectively, while the gain crossover and phase crossover frequencies are quite close to each other, at 318.7 rad/s and 318.4

Table 2. Closed-loop system poles and damping

Eigenvalue	Damping	Freq. (Rad/s)
-3.6746e+000+3.1722e+002i	1.1583e-002	3.1724e+002
-3.6746e+000-3.1722e+002i	1.1583e-002	3.1724e+002
-7.6507e+000	1.0000e+000	7.6507e+000

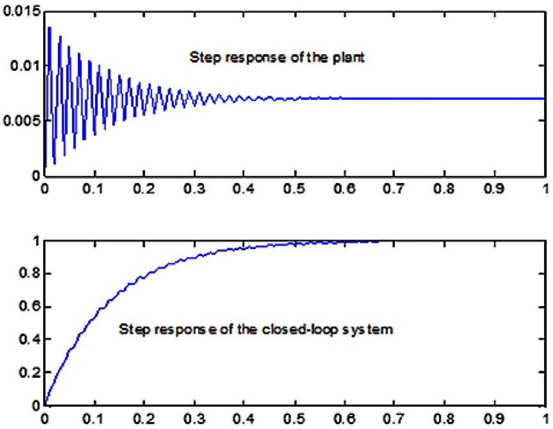

Figure 6. The step responses of the object and the microcontroller system with PI microcontroller for the opening-closing PV modules of a solar station

rad/s, respectively. It is clearly evident that the feedback system has less stability than the object.

In summary, the PI microcontroller not only produces a highly oscillatory response but also results in a significant loss of stability.

Efficient solar tracking strategies are essential to maximize surface exposure throughout the actuation path, and their performance has been thoroughly surveyed in recent literature [29–35].

Recent works confirm that PID microcontroller-based optimization in PV mechatronic actuation can effectively reduce steady-state error and high-frequency oscillations [25–26].

RESULTS AND DISCUSSION

Simulation and calculation of the PID microcontroller

To evaluate the effectiveness of the proposed PID controller, simulations were conducted and compared with the open-loop system. The goal was to reduce oscillations, improve positioning time, and ensure zero steady-state error.

Now, let's try to improve the PID microcontroller by selecting values for K_D, K_P, and K_I that will produce the desired response for the feedback system. It is preferable to have a feedback system with a good damping coefficient to reduce the number of oscillations and positioning time. Therefore, let's choose a damping coefficient $\zeta = 0.707$ for the feedback system while keeping the object's natural frequency unchanged at $\omega_n = 316.23$ rad/s. The general transfer function without feedback can be written as given in Equation 6.

$$G_v(s)C(s) = 700\left(K_D s^2 + K_p s + K_I\right)/ \\ /[s(s^2 + 15s + 100000)] \quad (6)$$

Note that the type of the microcontroller system has increased from 0 to 1 due to the presence of a pole at s = 0 in $G_v(s)$. Therefore, the steady-state error for a step input signal will be zero, regardless of the values of K_D, K_P, and K_I. The transfer function of the microcontroller system is given by $\frac{G_v(s)C(s)}{[1 + G_v(s)C(s)]}$ and can be expressed in the rational form $\frac{N(s)}{D(s)}$ as given in Equation 7,

$$N(s) = 700\left(K_D s^2 + K_p s + K_I\right); \\ D(s) = s^3 + (15 + 700K_D)s^2 + \\ +\left(100000 + 700K_p\right)s + 700K_I \quad (7)$$

where: $N(s)$ is the numerator and $D(s)$ is the denominator.

Note that the feedback system is of the third order. We can represent D(s) as the product of a quadratic factor and a first-order polynomial, which can be written as shown in Equation 8.

$$D(s) = (s^2 + 2\zeta\omega_n s + \omega_n^2)(s + p) \quad (8)$$

Note that in the transient (or impulse) response of the system, the poles with the smallest real parts dominate. If we select the two poles of the closed-loop system, obtained from the equation $(s^2 + 2\zeta\omega_n s + \omega_n^2)$, such that they are closer to the imaginary axis than the third pole s = –p, then the system response will be primarily influenced by the quadratic factor of D(s). The term (s + p) will have less effect on the closed-loop system's response. In this case, the roots of the equations $(s^2 + 2\zeta\omega_n s + \omega_n^2)$ are called the dominant poles of the closed-loop system. Since we have already chosen the damping coefficient $\zeta = 0.707$ and the natural frequency $\omega_n = 316.23$ rad/s for the closed-loop system, the pole s = -p in the left half-plane can be selected so that it is farther from the imaginary axis and satisfies the condition $p > \zeta\omega_n$ (e.g., p>223.57). Assuming p = 300, substituting the values of ζ, ω_n, and p into Eq. (8) and comparing it with the formula for *D*(*s*), we obtain the following PID microcontroller coefficients: $K_I = 42857.1$, $K_D = 1.0459$, $K_P = 191.64$. These values are the optimized PID controller coefficients, calculated to achieve critical damping and fast response with zero steady-state error for the microcontroller system. These values will result in the desired dynamics for the closed-loop system. The transfer function of the PID microcontroller can be expressed as given in Equation 9

$$C(s) = (1.0459s^2 + 191.64s + +42857.14)/s \tag{9}$$

Using the optimized PID controller, the transfer function of the resulting closed-loop system can be written as shown in Equation 10,

$$\frac{\omega(s)}{\omega_d(s)} = \frac{732.15s^2 + 134140s + 3x10^7}{(s+300)\left(s^2 + 447.15s + 100000\right)} \tag{10}$$

The step response of the closed-loop system can be calculated using the following commands:

- >>nCL=[732.15 134140 3e7];dCL = conv ([1 300], [1 447.15 1e5]);
- >>[s, t] = stepresp (nCL, dCL, 0,0.0005,0.03); plot(t,s);

As a result, the step response of the closed-loop system is shown in Figure 7. It is worth noting that the settling time is 0.025 seconds (compared to 0.7 seconds for the object), and high-frequency oscillations are completely absent, while ensuring zero steady-state error. Therefore, the characteristics of the object improve drastically due to the introduction of the PID microcontroller. Thus, the reliability margins of the closed-loop system containing the PID microcontroller, both in terms of gain margin and phase margin, can be calculated as follows:

- >> [gmCL,pmCL,wgCL,wpCL]=margin (GCL)
- gmCL = Inf, pmCL = 144.8923, wgCL = NaN, wpCL = 583.5848

The comparative performance of the system under different control strategies is summarized in Table 3.

It was found that the gain margin of the closed-loop system is infinite, while the phase margin is 144.9°, occurring at a gain crossover frequency of 583.6 rad/s. Although the phase margin is no longer infinite, as it was for the object, it is still quite large and sufficient. The large value of the gain crossover frequency indicates a very fast response, which is evident in Figure 7.

As shown in Figure 7, the PID controller significantly improves the dynamic response of the system. The settling time is reduced from 0.7 s to 0.025 s, and high-frequency oscillations are eliminated. These results confirm the theoretical predictions and demonstrate the effectiveness of the proposed control strategy.

It can be concluded that the closed-loop system with a PID microcontroller has a good combination of characteristics and stability. The Bode diagrams of the PID controller and the closed-loop system have been compared with the object's diagram in Figure 8.

It should be noted that the gain factor of the PID microcontroller exhibits a decreasing behavior at lower frequencies and an increasing behavior at higher frequencies. The PID microcontroller also introduces phase lag at frequencies

Table 3. Comparative performance of the system under different control strategies

Parameter	Open-loop	PI controller	PID controller
Settling time (s)	0.7	0.7	0.025
Steady-state error	≠ 0	0	0
Overshoot	High	Medium	Low
Stability margin	∞	Low	High

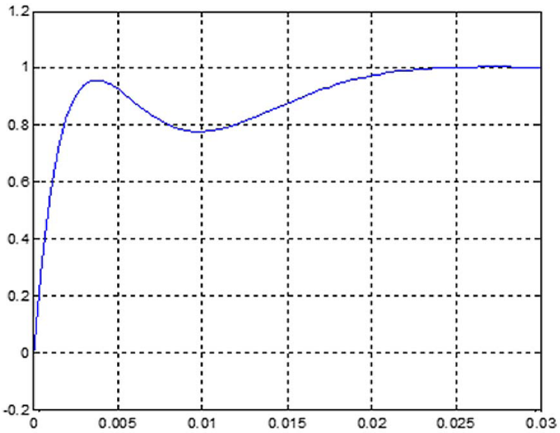

Figure 7. The step response of the closed-loop system with a PID microcontroller

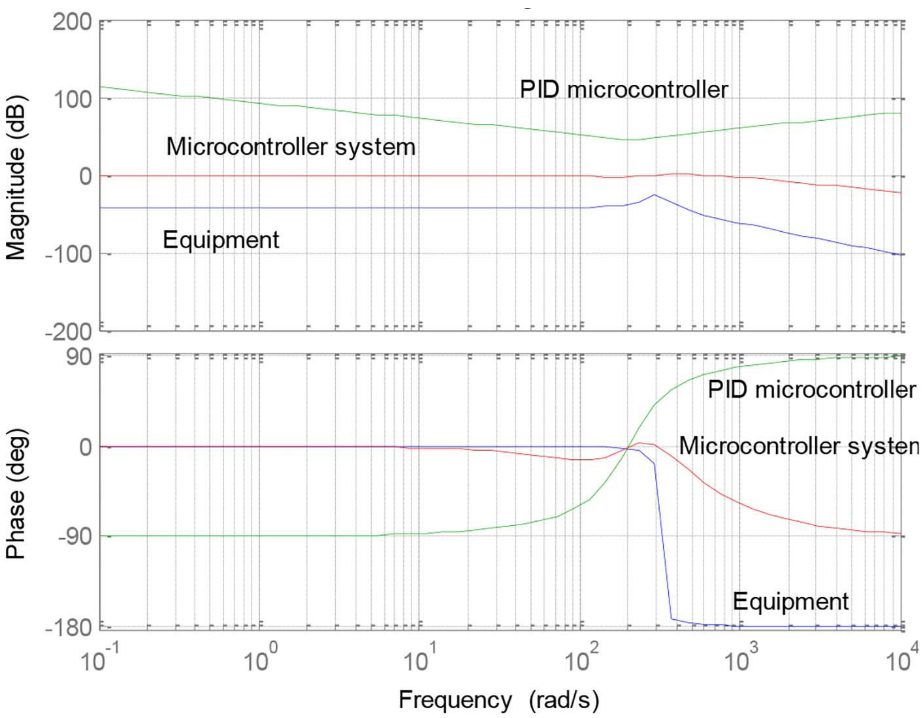

Figure 8. Bode diagrams of the equipment, the PID microcontroller, and the microcontroller system

lower than the system's natural frequency and phase lead at higher frequencies. As a result, the gain and phase diagrams of the closed-loop system are smoother compared to the system's open-loop diagram. However, due to the increased gain at higher frequencies, there is a small risk of increased sensitivity to high-frequency measurement noise, which is undesirable.

The Bode diagrams in Figure 8 further validate the improved performance of the PID-controlled system. Although the gain at high frequencies increases, which may introduce sensitivity to measurement noise, the overall phase margin and stability are significantly enhanced. Therefore, the PID controller offers a balanced trade-off between high-speed and robustness.

Future work will focus on the hardware implementation of the proposed PID-controlled actuation system and real-time control validation under practical operating conditions. In addition, the development of advanced adaptive or nonlinear control architectures is envisaged to further enhance robustness under varying load conditions and external disturbances. Experimental investigation of the interaction between folding dynamics and solar energy output could also provide valuable insights for optimizing photovoltaic deployment strategies in practical mobile environments.

CONCLUSIONS

This work presented a comprehensive design, modeling, and control analysis of a solar station equipped with automatically PV modules, driven by a microcontroller-based actuation system. A complete kinematic and dynamic representation of the folding mechanism was developed, allowing precise evaluation of system behavior under different control strategies. The results demonstrated that the proposed PID controller significantly improves the performance of the system compared to both the open-loop configuration and the PI-controlled case.

The simulation outcomes revealed substantial enhancements in transient and steady-state performance. Specifically, the PID controller reduced the settling time from 0.7 s to 0.025 s, fully eliminated high-frequency oscillations, and ensured zero steady-state error. These improvements were further validated by Bode diagram analysis, which showed that the optimized controller provides a high phase margin (144.9°) and infinite gain margin, indicating strong robustness and reliable operation even under dynamic actuation conditions. The comparison with the PI controller confirmed that the latter introduces oscillatory behavior and reduces stability, while the PID architecture overcomes these limitations by offering a better balance between response speed, stability, and vibration suppression.

Beyond the numerical improvements, the proposed control framework demonstrates high potential for integration into mobile solar platforms, including robotic systems, compact renewable-energy devices, and next-generation electric vehicles. The folding mechanism, combined with intelligent control, enables increased energy-harvesting efficiency while maintaining aerodynamic compactness and improving overall mobility. These qualities make the system particularly suitable for autonomous applications where adaptive geometry, fast reconfiguration, and efficient power management are essential.

It should be noted that this opening-closing equipment also allows for cleaning solar modules from dirt and snow. This is due to the centrifugal forces generated by the rotational motion of the solar modules.

REFERENCES

1. Haase G, Kirakossian G.T, Kirakosyan G.H, Mkrtchyan V.A. Designing optimal solar water pumping stations for irrigation of agricultural lands. Sci. Rev. Eng. and Environ. Sci. 2023;32(3):270–283.
2. Madhiarasan M. Design and development of an IoT-based solar-powered versatile moving robot for military applications. Int. Journ. Of Syst. Assur. Eng. and Manag. 2021;12:437–450. https://doi.org/10.1007/s13198-021-01089-9
3. Rao V, Surendra G, Teja A.Y, Ram P.E, Ravi C. Solar powered multipurpose military robot. Int. Journ. of Res. And Anal. Rev. 2019;6(1):837–878.
4. Kirakosyan G.H, Avetisyan K.A, Melkonyan V.S, Poghosyan A.G, Potikyan M.G. Design of a control system for a tracked robot using MATLAB package. Crisis Management and Technol. 2023;1(22):64–71 (in Russian).
5. Kirakosyan G.H, Vardanyan R.R, Shirinyan P.H, Machyan A.A. Solar PV modules automated cleaning system. In Proceedings of the 7th International Renewable and Clean Energy Conference; 27 Nov 2020; Yerevan, Armenia. p. 75–76.
6. Kirakosyan G.H, Melkonyan V.S, Avetisyan K.A. Design of the control system for the unmanned aerial vehicle by MATLAB system. Bull. Of High Technol. 2022;2(21):37–46.
7. Kirakosyan G.H, Avetisyan K.A, Potikyan M.G. Design of the control system for the unmanned aerial vehicle by MATLAB system. Crisis Manag. and Technol. 2022;2(21):22–32.
8. Kirakosyan G.H, Kamalyan A.G, Avetisyan K.A. Development of water resource control microprocessor system for PV pumping station. Crisis Management and Technol. 2024;1(24):119–126.
9. Kirakosyan G.H, Kamalyan A.G. Developing a microprocessor system for water level control in the reservoir. Bull. of Nat. Polytech. Univ. of Armenia. Part 1. 2024:76–83.
10. Li H, You B, Chen Y. Dynamic modeling and optimization of movable photovoltaic modules for electric vehicle charging. Appl. Energy. 2023;335:121238. https://doi.org/10.1016/j.apenergy.2023.121238
11. Kulkarni A, Keny J. Robotic solar power harvesting platform with foldable PV panels for maneuverability enhancement. Int. Journ. of Comput. Appl. 2022;184(46):12–18.
12. Kirakosyan G.H, Avetisyan K.A, Kamalyan A.G. Development of a microprocessor control system for a tracked mobile robot. Bull. of National Polytech. Univ. of Armenia. Part 1. 2023:94–101 (in Russian).
13. Kirakosyan G.H, Qamalyan A.G, Margaryan V.V, Khachaturyan V.G. Developing a controller algorithm for the charger in the grid-connected PV system. Bull. of National Polytech. Univ. of Armenia. Part 1. 2019:183–192.
14. Kirakosyan G.H, Khachaturyan V.G, Kirakosyan L.G. Modeling and design of a DC motor with a PID controller by MATLAB software. Bull. of National Polytech. Univ. of Armenia. Part 1. 2016:98–104.
15. Kirakosyan G.H, Melkonyan V.S. Cleaning head controller for photovoltaic panel. In Proceedings of the International Symposium on Embedded Systems and Trends in Teaching Engineering; 11–15 Sep 2016; Nitra, Slovakia. p. 65–71.
16. Kirakosyan G.H, Verlinski S.V, Alaverdyan A.S. An automatic cleaning system for solar panels. Bull. of National Polytech. Univ. of Armenia. Part 1. 2017:156–161 (in Russian).
17. Kirakosyan G.H, Alaverdyan A.S, Petrosyan R.P, Khachatryan H.G. A chopper with the control system based on a digital processor. Proc. NPUA: Inf. Technol., Electron., Radio Eng. 2018;(1):82–88.
18. Sahu A, Chauhan P, Singh A. Performance analysis of a small-scale solar tracking system using PID controller. Mater. Today: Proc. 2021;47:5591–5596.
19. Kirakosyan G.H, Ayvazyan G.Y, Vardanyan A.H. Maximum power point tracker for the PV water pumping system. In Proceedings of the 3rd International Renewable and Clean Energy Conference; 27–29 Jun 2007; Yerevan, Armenia. p. 26–27.
20. Kirakosyan G.H, Avetisyan K.A, Kondjoryan A.H, Kirakosyan L.G. Simulation and construction of a fuzzy-based maximum power point tracker for solar energetic plants. Proc. Engineering Academy of Armenia. 2014;11(1):135–141.

21. Kirakosyan G.H, Khachaturyan V.G, Barseghyan V.D, Torosyan L.Y. Developing a controller for wind power plants. Bulletin of National Polytechnic University of Armenia. Part 1. 2015:91–96.
22. Kirakosyan G.H, Alaverdyan A.S, Khachaturyan V.G, Vardanyan R.R. Remote monitoring system for parameters of solar water pumping stations. Bulletin of National Polytechnic University of Armenia. Part 1. 2018:85–90 (in Russian).
23. Kirakosyan G.H, Melkonyan V.S, Margaryan V.V, Kirakosyan L.G. Modeling and simulation of MPPT for grid-connected PV system. Proc. NPUA: Information Technologies, Electronics, Radio Engineering. 2018;(2):30–40.
24. Kirakosyan G.H, Khachaturian V.G, Kirakosyan L.G, Avetisyan K.A. Developing a controller for a photovoltaic system by neural networks. Bulletin of National Polytechnic University of Armenia. Part 2. 2021:284–294.
25. Dorf R.C, Bishop R.H. Modern Control Systems. New York: Prentice Hall; 2011.
26. Jasim F.C, Hammoodi A.I. Implementation of PID control to reduce oscillation in photovoltaic mechatronic systems. Energy Rep**.** 2022;8:5575–5583. https://doi.org/10.1016/j.egyr.2022.04.032
27. Gilat A. MATLAB: An Introduction with Applications. New York: John Wiley & Sons; 2018.
28. Kirakosyan G.H, Melkonyan V.S, Avetisyan K.A. Control system design for an unmanned aerial vehicle using MATLAB. Bulletin of High Technology. 2022;2(21):37–46.
29. Fouad M.M, Shihata M, Shabana M. Solar tracking systems: technologies and track records. Renew. And Sustain. Energy Rev. 2022;153:111787. https://doi.org/10.1016/j.rser.2021.111787
30. Kirakosyan G.H, et al. Control of the heliotracker of a solar power plant. Proc. NAS RA & NPUA, Ser. Tech. Sci. 2017;70(3):333–340 (in Russian).
31. Wang J.M, Lu C.L. Design and implementation of a sun tracker with a dual-axis single motor for an optical sensor-based photovoltaic system. Sensors. 2013;13:3157–3168. https://doi.org/10.3390/s130303157
32. Axaopoulos P.J. Energy and economic comparative study of a tracking vs. a fixed PV system. Eur. Sci. Jour. 2013;9(12):50–58.
33. Lave M, Kleissl J. Optimum fixed orientations and benefits of tracking for capturing solar radiation in the continental United States. Renew. Energy. 2011;36:1145–1152. https://doi.org/10.1016/j.renene.2010.07.032
34. Li Z, Liu X, Tang R. Optical performance of vertical single-axis tracked solar panels. Renew. Energy. 2011;36:64–68. https://doi.org/10.1016/j.renene.2010.05.020
35. Ayvazyan K.G. High-efficiency solar cells and stations. Yerevan: Gasprint; 2016.